

IEEE

GEOSCIENCE AND REMOTE SENSING LETTERS

A PUBLICATION OF THE IEEE GEOSCIENCE AND REMOTE SENSING SOCIETY



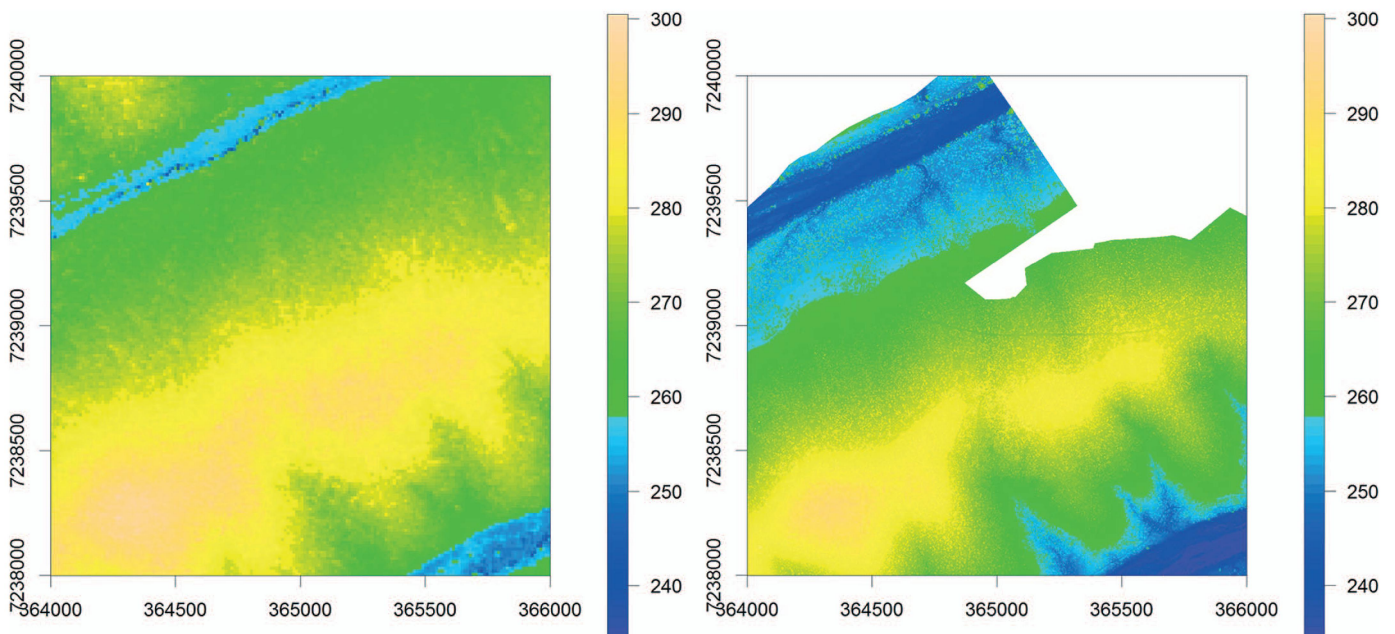
FEBRUARY 2016

VOLUME 13

NUMBER 2

IGRSBY

(ISSN 1545-598X)



(Left) Tandem-X intermediate DEM over Sabie Sands Peninsula in Kruger National Park, South Africa.
(Right) Last return height from airborne LiDAR. Units are in meters.

IEEE

GEOSCIENCE AND REMOTE SENSING LETTERS

A PUBLICATION OF THE IEEE GEOSCIENCE AND REMOTE SENSING SOCIETY



FEBRUARY 2016

VOLUME 13

NUMBER 2

IGRSBY

(ISSN 1545-598X)

PAPERS

Atmosphere

Estimation of the Atmospheric Mean Radiating Temperature Throughout the World in a Nonscattering Atmosphere . . .	<i>M. J. Lucas-Vegas and J. M. Riera</i>	167
An Algorithm for Wind Direction Retrieval From X-Band Marine Radar Images	<i>Y. Wang and W. Huang</i>	252

Oceans and Water

Evaluation of Sea Surface Temperature From FY-3C VIRR Data in the Arctic.	<i>H. Wang, L. Guan, and G. Chen</i>	292
---	--------------------------------------	-----

Cryosphere

On the Interpretation of Polarimetric Phase Differences in SAR Data Over Land Ice	<i>G. Parrella, I. Hajnsek, and K. P. Papathanassiou</i>	192
---	--	-----

Surface and Subsurface Properties

Automatic Arc Distortion Correction of Seismograms Using the Low-Rank Matrix Recovery Method	<i>L. Wang, R. Liu, and Y. Sun</i>	142
Simultaneous-Source Separation Using Iterative Seislet-Frame Thresholding.	<i>S. Gan, S. Wang, Y. Chen, and X. Chen</i>	197

Image Processing, Analysis and Classification

Efficient Saliency-Based Object Detection in Remote Sensing Images Using Deep Belief Networks	<i>W. Diao, X. Sun, X. Zheng, F. Dou, H. Wang, and K. Fu</i>	137
An Informative Feature Selection Method Based on Sparse PCA for VHR Scene Classification	<i>S. Chaib, Y. Gu, and H. Yao</i>	147
Unsupervised Multilayer Feature Learning for Satellite Image Scene Classification.	<i>Y. Li, C. Tao, Y. Tan, K. Shang, and J. Tian</i>	157
Relative Radiometric Normalization for Multitemporal Remote Sensing Images by Hierarchical Regression	<i>C. Zhong, Q. Xu, and B. Li</i>	217
PolSAR Image Classification via D-KSVD and NSCT-Domain Features Extraction	<i>W. Xie, L. Jiao, and J. Zhao</i>	227
Infrared Target Tracking Based on Robust Low-Rank Sparse Learning	<i>Y. He, M. Li, J. Zhang, and J. Yao</i>	232
Mapping Indoor Spaces by Adaptive Coarse-to-Fine Registration of RGB-D Data	<i>D. R. dos Santos, M. A. Basso, K. Khoshelham, E. de Oliveira, Jr., N. L. Pavan, and G. Vosselman</i>	262

(Contents Continued on Page 122)



Hyperspectral Data Processing	
Low-Rank Decomposition Model for Adaptive Identification of Similar Neighboring Pixels in Hyperspectral Images	<i>F. Chen, T. F. Tang, and K. Wang</i> 172
Hyperspectral Image Classification via JCR and SVM Models With Decision Fusion.	<i>C. Bo, H. Lu, and D. Wang</i> 177
Radar Systems	
Extraction of Human Micro-Doppler Signature in an Urban Environment Using a ‘‘Sensing-Behind-the-Corner’’ Radar	<i>M. Gustafsson, Å. Andersson, T. Johansson, S. Nilsson, A. Sume, and A. Örbom</i> 187
Array Factor Forming for Image Reconstruction of One-Dimensional Nonuniform Aperture Synthesis Radiometers	<i>L. Feng, M. Wu, Q. Li, K. Chen, Y. Li, Z. He, J. Tong, L. Tu, H. Xie, and H. Lu</i> 237
First Demonstration of Airborne SAR With Nonlinear FM Chirp Waveforms.	<i>W. Wang, R. Wang, Z. Zhang, Y. Deng, N. Li, L. Hou, and Z. Xu</i> 247
CFAR Detection of Moving Range-Spread Target in White Gaussian Noise Using Waveform Contrast	<i>X. Yang, G. Wen, C. Ma, B. Hui, B. Ding, and Y. Zhang</i> 282
Microwave Radiometry	
Study of Variability of Complex Permittivity of Terrestrial Analogue of Lunar Soil (TALS) Having Different Percentage of Water at Microwave Frequencies	<i>O. P. N. Calla, S. Mathur, and K. Lal Gadri</i> 123
A Scheme to Measure Lateral Velocity by Radio Interferometry.	<i>C. Li, Z. Chen, and X. Wu</i> 127
Microwave Brightness Temperature of the Moon: The Possibility of Setting a Calibration Source of the Lunar Surface	<i>G.-P. Hu, Y.-C. Zheng, A.-A. Xu, and Z. Tang</i> 182
Improvement of Data Precision and Spatial Resolution of cGNSS-R Altimetry Using Improved Device With External Atomic Clock.	<i>L. Bao, N. Wang, and F. Gao</i> 207
Synthetic Aperture Radar	
SAR Image Segmentation Using the Roughness Information	<i>F. A. Ávila Rodrigues, J. F. S. Rocha Neto, R. C. Pinheiro Marques, F. N. Sombra de Medeiros, and J. Santos Nobre</i> 132
Radar/SAR Image Resolution Enhancement via Unifying Descriptive Experiment Design Regularization and Wavelet-Domain Processing	<i>Y. V. Shkvarko, J. I. Yañez, J. A. Amao, and G. D. Martín del Campo</i> 152
Demonstration of Single-Pass Millimeterwave SAR Tomography for Forest Volumes.	<i>M. Schmitt and X. Xiang Zhu</i> 202
Ship Classification in SAR Image by Joint Feature and Classifier Selection	<i>H. Lang, J. Zhang, X. Zhang, and J. Meng</i> 212
SAR Target Configuration Recognition Using Tensor Global and Local Discriminant Embedding	<i>X. Huang, H. Qiao, and B. Zhang</i> 222
Feature-Area Optimization: A Novel SAR Image Registration Method.	<i>F. Liu, F. Bi, L. Chen, H. Shi, and W. Liu</i> 242
Detection of Durable and Permanent Changes in Urban Areas Using Multitemporal Polarimetric UAVSAR Data	<i>D. Kim, S. Hensley, S.-H. Yun, and M. Neumann</i> 267
Measuring 3-D Surface Motion With Future SAR Systems Based on Reflector Antennae	<i>H. Ansari, F. De Zan, A. Parizzi, M. Eineder, K. Goel, and N. Adam</i> 272
Validation of the TanDEM-X Intermediate Digital Elevation Model With Airborne LiDAR and Differential GNSS in Kruger National Park	<i>H. Balzter, J. Baade, and K. Rogers</i> 277
An Extension of a Complete Model-Based Decomposition of Polarimetric SAR Data.	<i>F. Zhu, Y. Zhang, and D. Li</i> 287
Lidar Systems	
Accelerated Coherent Point Drift for Automatic Three-Dimensional Point Cloud Registration	<i>M. Lu, J. Zhao, Y. Guo, and Y. Ma</i> 162
Planar Segmentation Using Range Images From Terrestrial Laser Scanning.	<i>G. Zhou, S. Cao, and J. Zhou</i> 257

About the Cover: The TanDEM-X mission is providing a global digital elevation model (DEM) from a bistatic satellite constellation using synthetic aperture radar (SAR) interferometry. Two radar satellites are mapping the Earth aiming for an absolute height error of <10 m and a relative height error of <2 m for 90% of the elevation data. An intermediate DEM (IDEM) with reduced accuracy was produced from the first coverage. The figure shows a validation of the IDEM product with airborne LiDAR over a savanna site on Sabie Sands Peninsula in Kruger National Park, South Africa. (Left) Tandem-X intermediate Digital Elevation Model (IDEM). (Right) Last return height from airborne LiDAR. Units are in meters. For more information please see ‘‘Validation of the TanDEM-X Intermediate Digital Elevation Model With Airborne LiDAR and Differential GNSS in Kruger National Park,’’ by Balzter *et al.*, which begins on page 277.